



Cu atoms on UiO-66-NH₂/ZnIn₂S₄ nanosheets enhance photocatalytic performance for recovering hydrogen energy from organic wastewater treatment

Sijia Liu^a, Xifei Zhou^a, Changqing Yang^a, Chaochai Wei^{a,b,c}, Yun Hu^{a,b,c,*}

^a School of Environment and Energy, South China University of Technology, Guangzhou 510006, PR China

^b Guangdong Provincial Engineering and Technology Research Centre for Environmental Risk Prevention and Emergency Disposal, Guangzhou 510006, PR China

^c The Key Lab of Pollution Control and Ecosystem Restoration in Industry Clusters, Ministry of Education, Guangzhou 510006, PR China

ARTICLE INFO

Keywords:

Synergetic photocatalysis
Hydrogen production
Organic pollutants degradation
Cu atoms
UiO-66-NH₂

ABSTRACT

The extensive use of sacrificial agents and the low carrier separation and utilization efficiency remain important factors limiting the development of photocatalytic hydrogen production. We report a three-layered, dual-functional photocatalysts of Cu atoms@UiO-66-NH₂(U6N)/ZnIn₂S₄ nanosheets (ZIS), for the simultaneous production of photocatalytic hydrogen and degradation of organic pollutants. When common and highly toxic organic pollutants (phenolic compounds and antibiotics) were substituted for the sacrificial agents, Cu@U6N/ZIS exhibited superior sustained hydrogen production, approximately 28 times greater than that of pure ZIS. The experimental results suggested that the window size of U6N (< organic pollutants molecular size) separates the reaction sites of organic pollutants oxidation and reduction of hydrogen ions (H⁺), thereby achieving spatial separation of redox sites. Besides, the structure of Cu@U6N/ZIS, which was anchored Cu within U6N and encapsulated by ZIS nanosheets, forming Z-type heterojunctions, achieved the control of the directional transfer of photogenerated electrons. And the coupled system can effectively enhance water quality by reducing the biological toxicity of the wastewater. This study suggests new avenues for environmental restoration and non-fossil fuel production.

1. Introduction

Photocatalytic hydrogen production is a promising solution to the energy crisis [1–3]. However, in current photocatalytic hydrogen production systems, a sacrificial agent, such as methanol, ethanol, and triethanolamine, must be introduced [4,5]. These materials are expensive, toxic, and harmful to the environment, and they are originally energy carriers [6]. Coupling photocatalytic degradation of organic pollutants with hydrogen production is an economical and sustainable solution to utilize the holes left by the consumption of electrons during hydrogen evolution and also to replace the role of sacrificial agents in promoting hydrogen production. Further, pollutants and their partial degradation products are potential electron sources that can be used for reducing H⁺ by photogenerated electrons [7].

Many organic pollutants pose risks to the environment and public health. Among problematic pollutants are phenols and phenolic compounds that are widely found in wastewater of chemical plants and are

resistant to degradation [8,9]. In particular, the increased use of antibiotics and their subsequent release into the environment have raised legitimate concerns in recent years [10,11]. Environmental degradation of these organic pollutants is limited, in part, by their designed high toxicity to microorganisms [12].

Traditional physical and chemical water treatment methods (e.g., sedimentation, filtration, adsorption) are expensive to operate and are often insufficient to ensure good quality water [13,14]. In contrast, photocatalytic methods have been successful in treating multiple harmful organic pollutions by converting them into easily biodegradable and less toxic compounds [15].

Although many reports have focused on the photocatalytic degradation of organic pollutants, the overlap of oxidation and reduction sites in coupled systems has largely gone unstudied, which ignores a possibly significant synergistic photocatalytic reaction pathway. To couple these two systems, it is important to develop highly efficient dual-functional photocatalysts that have more active reaction sites for oxidation and

* Corresponding author at: School of Environment and Energy, South China University of Technology, Guangzhou 510006, PR China.

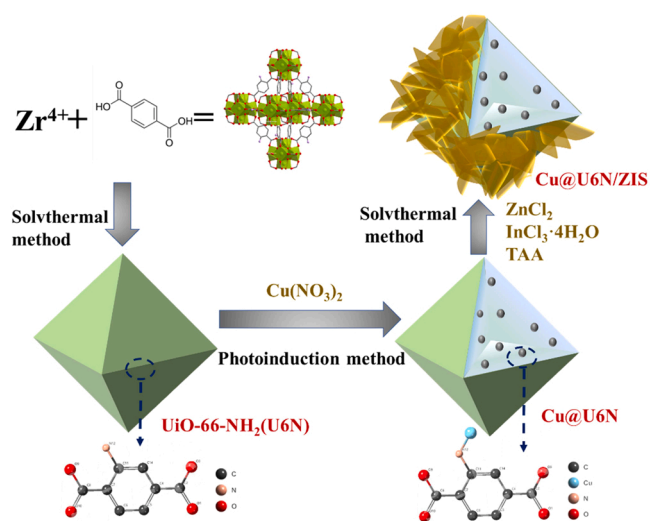
E-mail address: huyun@scut.edu.cn (Y. Hu).

<https://doi.org/10.1016/j.apcatb.2023.122572>

Received 8 February 2023; Received in revised form 27 February 2023; Accepted 3 March 2023

Available online 4 March 2023

0926-3373/© 2023 Elsevier B.V. All rights reserved.



Scheme 1. Synthesis diagram of Cu@U6N/ZIS.

for reduction.

MOF materials with tunable pore structures and functional modifiable framework structures represent a promising class of candidate materials for use in photocatalytic reactions [16–18]. For example, MOFs (e.g., UiO-66, NTU-9, MOF-5) have properties like semiconductors and can generate charge carriers by photoexcitation of metal clusters or organic ligands [19,20]. However, a pure MOF generally does not absorb much visible light, and the electron-hole pairs that are created are easily and quickly recombined since they are created in close proximity to each other [21,22]. The design and development of a Z-type heterojunction between two semiconductors can effectively facilitate charge transfer by separating the sites of photoelectron generation and hole formation, thereby enhancing redox capability [23–25]. For example, ZnIn_2S_4 , which has a strong visible light absorption and high stability, is a good choice for the construction of heterojunctions with MOF [26,27]. Owing to the layered crystal structure of ZnIn_2S_4 , it tended to form an ultrathin 2D nanomaterials [28], and the separation efficiency of electron-hole pairs was greatly promoted. In addition, the 2D nanosheets morphology of ZnIn_2S_4 allowed an intimate contact interface with the MOF [29], increasing the contact surface area and facilitating material exchange and electron transport.

In addition, the pore spaces in MOF can act as ordered nanoreactors [30]. That is, noble metals and metal complexes have been incorporated within porous channels MOFs are used to improve their photocatalytic performance [31–33]. Copper, a transition metal that is abundant in the earth and plays a special reducing role in a number of reported photocatalytic systems [34,35]. In addition, copper coordinates with various ligands and complexes with amino ($-\text{NH}_2$) moieties to form a reduction reaction center [36,37]. For example, the MOF complexed with amino terephthalic acid ligands contains a large number of $-\text{NH}_2$ moieties that serve as reaction sites.

Based on the above discussion, we have synthesized a three-layer dual-functional photocatalytic material Cu@U6N/ZIS to anchor Cu on U6N using a photoinduction method and added ZIS on the outside of the U6N by a hydrothermal method (Scheme 1). We present data here that characterize the Cu@U6N/ZIS as a three-layered structure containing Z-type heterojunctions that promote the separation of electrons and holes. Because of the size differences between the molecular diameter of organic pollutants and the size of the gaps in the U6N window, there is a separation between the site of the hydrogen evolution, on one hand, and organic pollutants oxidation sites, on the other, resulting in improved photocatalytic performance. The charge transfer pathway and possible photocatalytic mechanism of the coupled system are also discussed. The toxicity of the aquatic phenol solution was evaluated using *Chlorella*

vulgaris as an ecological indicator. The positive results of this study are an encouraging introduction to a new approach for developing hydrogen energy from wastewater.

2. Experimental section

2.1. Chemicals

Zirconium chloride (ZrCl_4), 2- NH_2 -terephthalic acid (H_2ATA), $\text{Zn}(\text{NO}_3)_2 \cdot 6\text{H}_2\text{O}$, ZnCl_2 , $\text{InCl}_3 \cdot 4\text{H}_2\text{O}$, and thioacetamide (TAA) were purchased from Aladdin Reagent Co., Ltd. (Shanghai, China). Acetic acid, N, N-dimethylformamide (DMF), methanol, and ethanol were obtained from Sinopharm Chemical Reagent Co., Ltd. (Shanghai, China). All chemicals and reagents were analytical grade and used as received without further purification. Deionized water was used in the experiment.

2.2. Materials

2.2.1. Preparation of UiO-66- NH_2

In a typical synthesis [38], 50 mL DMF solution of 0.2332 g ZrCl_4 and 0.1812 g of H_2ATA were mixed in a 100 mL Teflon-lined stainless steel autoclave. Subsequently, 6 mL acetic acid was added and sonicated for 10 min; the autoclave was sealed and heated at 120°C for 24 h under autogenous pressure. After cooling to room temperature, the precipitate was collected by centrifugation and rinsed with anhydrous methanol several times to remove residual DMF. Finally, the UiO-66- NH_2 was dried at 100°C under vacuum for 12 h.

2.2.2. Preparation of Cu@U6N

0.01 g of $\text{Cu}(\text{NO}_3)_2 \cdot 3\text{H}_2\text{O}$ was dissolved in 100 mL deionized water. UiO-66- NH_2 activated at 120°C for 12 h before use, was dispersed in the above solution, sonicated for 10 min, and constantly stirred for 3 h. After filtering, the pretreatment sample was dispersed again in a mixed solution of 20 mL ethanol + 80 mL water. The mixture was stirred with a magnetic stirrer while being illuminated under, a 300 W Xe lamp with a cutoff filter ($\lambda \geq 420\text{ nm}$) for 3 h. The suspension was filtered, washed, and dried at 100°C under vacuum for 12 h. The resulting hazel solid was labeled Cu@U6N.

2.2.3. Preparation of Cu@U6N/ZIS

100 mg Cu@U6N was dispersed in 40 mL DI water (pH = 2, adjusted by HCl) and sonicated for 20 min, followed by addition of 10 mL of glycerol and stirred for 30 min. Then, 136 mg of ZnCl_2 , 586 mg of $\text{InCl}_3 \cdot 4\text{H}_2\text{O}$, and 301 mg of thioacetamide (TAA) were dissolved in the above suspension while being stirred for 20 min. Next, the liquid was maintained at a temperature of 80°C and stirred for 3 h. After cooling to room temperature, the liquid was centrifuged, and the precipitate was collected and washed with ethanol three times. After drying at 80°C under vacuum for 12 h, the yellow-brown solid was denoted as Cu@U6N/ZIS. Pure ZIS was prepared as the control sample under the same reaction conditions without Cu@U6N. U6N/ZIS was prepared as stated above but with the Cu@U6N replaced by U6N.

2.3. Photocatalytic hydrogen production

Typically, 100 mg of the photocatalyst, 180 mL of H_2O , and 20 mL of triethanolamine (TEOA) were placed in a 400 mL top-irradiation quartz container (PQ256, Beijing) and irradiated with a 300 W Xe lamp equipped with a cutoff filter ($\lambda \geq 420\text{ nm}$) to simulate visible light. Prior to irradiation, the reaction system was vigorously stirred by a magnetic stirrer at a constant temperature (25°C) and bubbled with N_2 for 30 min to remove dissolved oxygen. Hydrogen gas produced was detected by gas chromatography (GC9790II, TCD detector, nitrogen gas carrier).

Phenolic compounds and antibiotics were chosen to represent organic pollutants in wastewater. The TEOA as an electron donor was

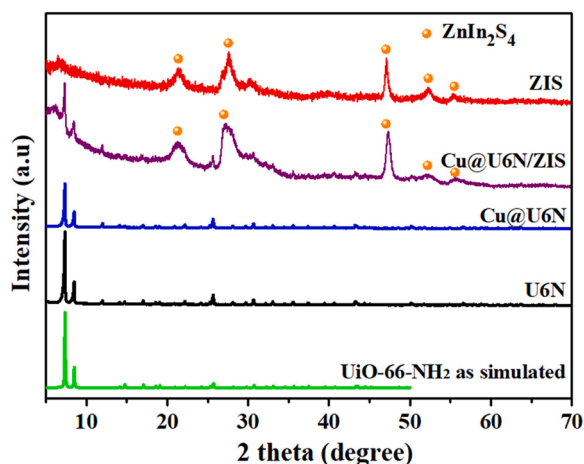


Fig. 1. XRD images of different samples.

replaced with different organic pollutants and other reaction conditions were the same as above. Before irradiation, the system was purged with nitrogen (N_2) and maintained in the dark for 30 min to reach adsorption equilibrium. The concentration of phenol was determined with a high performance liquid chromatography (HPLC, Shimadzu LC-20AT), equipped with a C18 (250×4.6 mm, Agilent) column. The phenol removal percent (η) was calculated as $\eta (\%) = (1 - C/C_0) \times 100\%$, where C_0 and C are the concentrations of phenol before and after reaction, respectively.

2.4. Characterizations

The crystal structures of the samples were determined using X-ray diffraction (XRD) with a Bruker D8 Advance diffractometer. The morphologies of the samples were characterized by scanning electron

microscopy (SEM, Hitachi S-4800, FE-SEM) and transmission electron microscopy (TEM, FEI Talos F200X). The functional groups of samples were determined using Fourier-transform infrared spectra (FT-IR, Nicolet-6700 FT-IR spectrometer) using KBr pellets. The surface chemical states of the samples were studied using X-ray photoelectron spectroscopy (XPS, Thermo Fisher Scientific, Escalab 250) equipped with an Al $K\alpha$ source. The specific surface areas of the samples were determined from N_2 adsorption-desorption isotherms at 77 K (Micromeritics ASAP 2020 M Analysis).

2.5. Assays of toxicity

The aquatic toxicity of phenol solution was assessed using *Chlorella vulgaris*. The medium of the control group was sterilized ultra-pure water without phenol, and the test groups used phenol solutions before and after photocatalytic treatment. The cell density of *Chlorella vulgaris* was determined every day with a UV-vis spectrometer by measuring the absorption of light at 680 nm.

3. Results and discussion

3.1. Characterization

The crystal structures of the ZIS, Cu@U6N/ZIS, Cu@U6N, and U6N were investigated by XRD (Fig. 1). The XRD peak of synthetic U6N was the same as the simulation results, indicating that the UiO-66-NH₂ was synthesized successfully. The characteristic peak of Cu@U6N was consistent with that of U6N, and no new peaks were generated, which indirectly indicated the low content and small size of Cu species. The XRD pattern of ZIS showed the characteristic diffraction peaks at 21.4° , 27.6° , 47.1° , 52.3° , and 55.7° corresponds to (006), (102), (110), (116), and (022) planes [32], which were in agreement with the typical structure of hexagonal $ZnIn_2S_4$ (JCPDS No.65-2023). For Cu@U6N/ZIS sample, the characteristic peaks of hexagonal $ZnIn_2S_4$ appeared, while

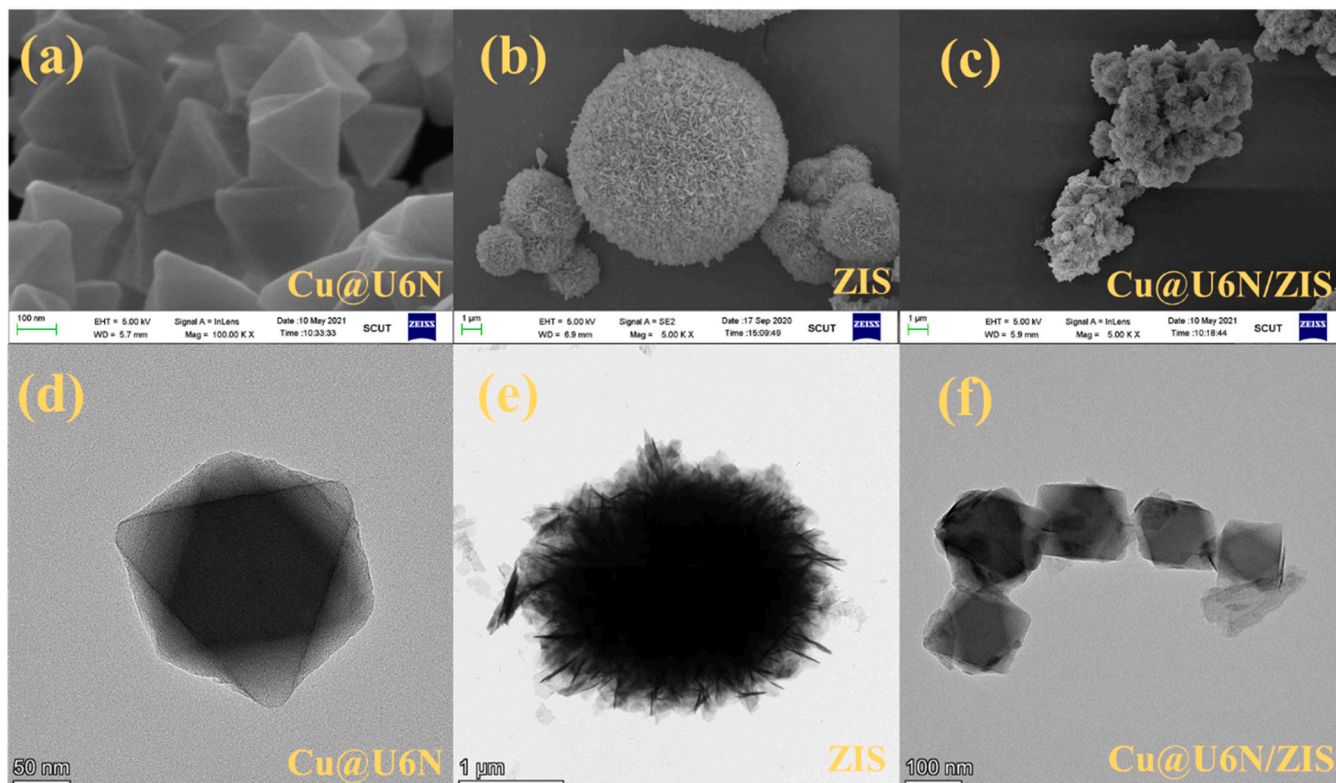


Fig. 2. SEM images of (a) Cu@U6N, (b) ZIS, and (c) Cu@U6N/ZIS; TEM images of (d) Cu@U6N, (e) ZIS and (f) Cu@U6N/ZIS.

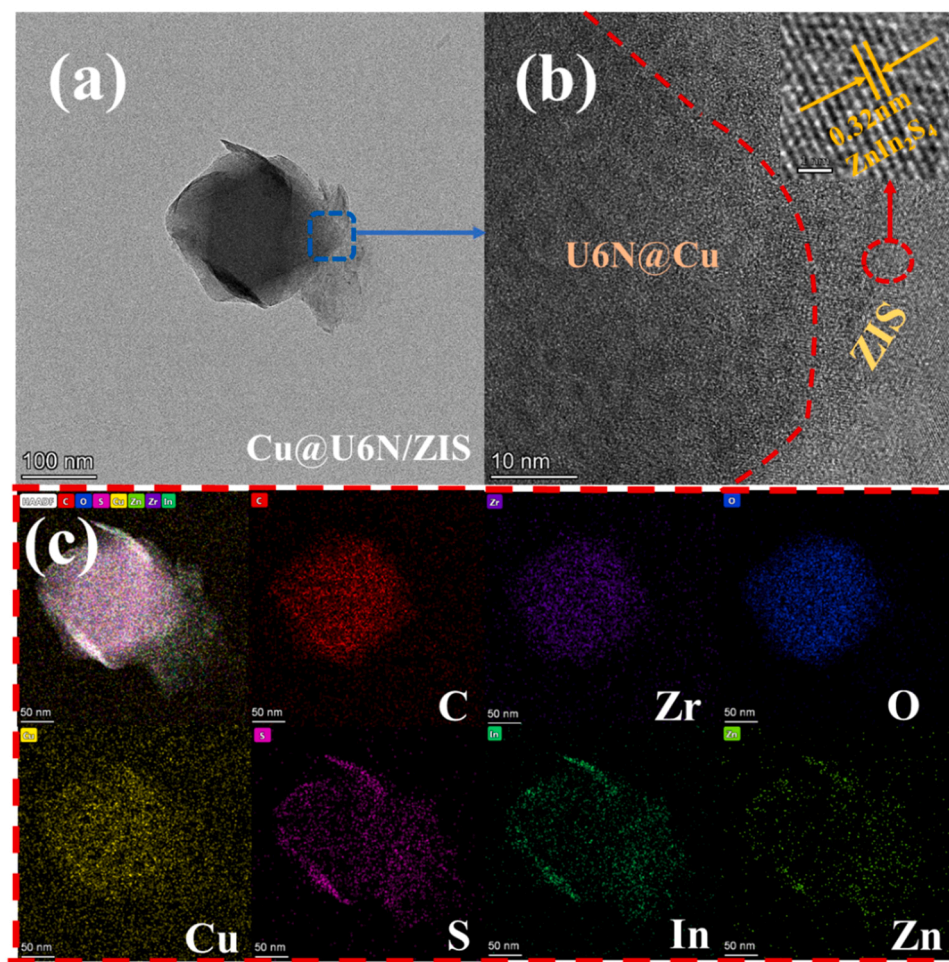


Fig. 3. (a) TEM image, (b) HRTEM image, and (c) EDS mappings of Cu@U6N/ZIS.

part of the diffraction peak of UiO-66-NH₂ was covered and could still be identified in the XRD pattern. The successful preparation of composite materials was confirmed.

From the scanning electron microscopy (SEM) image (Fig. S1a), U6N displayed a uniform octahedron structure with a smooth surface and an average edge length of approximately 200 nm. The U6N retained the octahedron structure even after Cu atoms were anchored on the U6N by a photoinduction method, (Fig. 2a). Transmission electron microscopy (TEM) revealed no Cu particles inside Cu@U6N (Fig. 2d). On the other

hand, the TEM-EDS image (Fig. S2) showed a uniform distribution of Cu atoms in the U6N. This confirmed the successful loading of highly dispersed Cu inside.

ZIS exhibited a microsphere morphology containing many interwoven nanosheets with a diameter of 1 ~ 3 μm (Fig. 2b and e). The images of Cu@U6N/ZIS obtained after in-situ growth of ZIS on Cu@U6N are shown in Fig. 2c and f. The outer surface of Cu@U6N was completely coated with very close wrinkled ZIS nanosheets. The Cu@U6N/ZIS nanocomposites displayed regular nanoclusters with tight

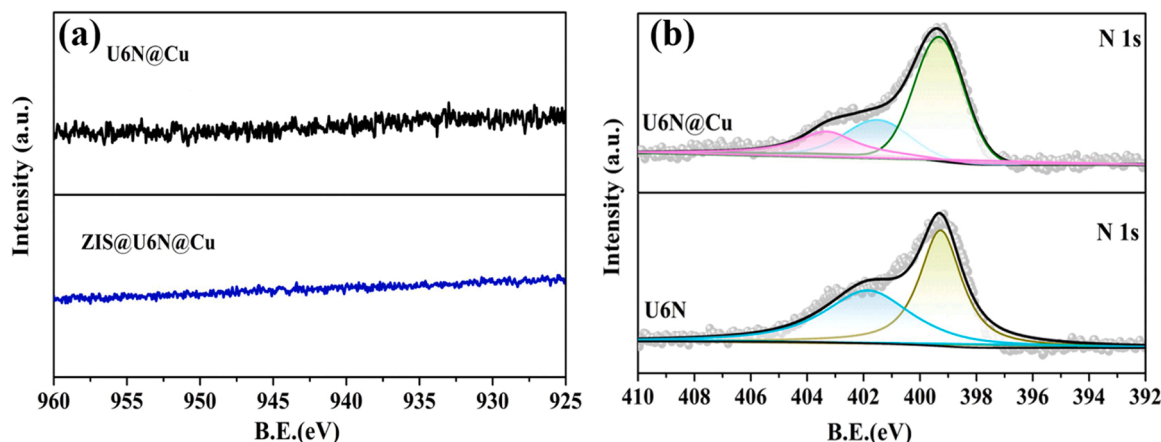


Fig. 4. XPS high-resolution scans of (a) Cu 2p, (b) N 1s.

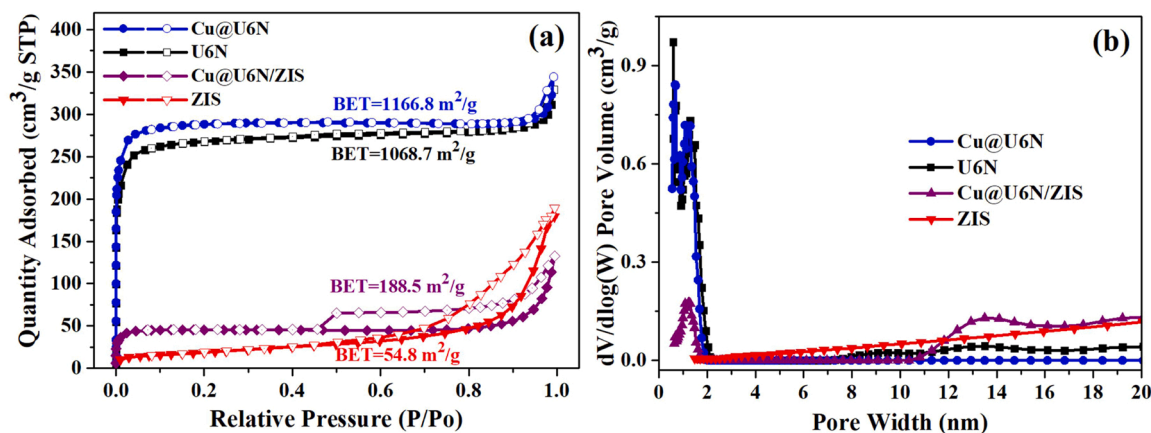


Fig. 5. (a) N_2 sorption isotherms of different samples, and (b) the corresponding pore size distributions calculated by the DFT model.

nanosheets decorated.

HRTEM images provided detailed information about the internal structure of Cu@U6N/ZIS nanocomposites (Fig. 3). There was a clear intimate contact interface between Cu@U6N and ZIS, which was marked by the red dotted line in Fig. 3b. Such contact would facilitate the transfer of photogenerated charge carriers between Cu@U6N and ZIS. The lamellar structure on the right of Fig. 3b show clear lattice fringes with an interface angle of 0.32 nm, corresponding to the (102) crystal plane of hexagonal $ZnIn_2S_4$. On the left side, no obvious Cu particles were observed in Cu@U6N, and no signal related to crystalline Cu species was found, which is consistent with a high dispersion of Cu species.

The elemental composition and spatial distribution of Cu@U6N/ZIS nanocomposites were studied by TEM-EDS mapping analysis, which confirmed that Cu@U6N/ZIS had a multilayer structure. As shown in Fig. 3c, Zr, O, C, Cu, S, In, and Zn elements are distributed in Cu@U6N/ZIS nanocomposites. Among them, Zr, O, and C elements were concentrated and distributed, and attributed to U6N. In addition, S, In, and Zn elements with depth color and distribution on the outside were attributed to ZIS. The distribution of Cu was superimposed on U6N, indicating that Cu@U6N/ZIS has a three-layer structure. The special structure of Cu@U6N/ZIS, which had anchored Cu in U6N and were encapsulated by ZIS nanosheets, allowed for control of the directional transfer of photogenerated electrons from the outside to the inside. Further, the real ratio of metal elements in the samples was determined by ICP-MS (Table S1).

To further confirm the binding pattern of Cu to U6N, Fourier transform infrared spectroscopy (FTIR) and X-ray photoelectron spectroscopy (XPS) were used to explore the surface elemental composition and chemical state of Cu@U6N/ZIS samples. During preparation, Cu species were first adsorbed within U6N which then formed from corresponding complexes with the $-NH_2$ groups through a photoinduction process. According to Fig. S3, the characteristic peaks at 1656 and 1062 cm^{-1} were contributed by $-NH_2$ groups in U6N [31]. These peaks changed in intensity and position of Cu@U6N, indicating that the Cu species interacted with the $-NH_2$ groups.

Similarly, the chemical states of N elements in U6N and Cu@U6N were examined by XPS (Fig. 4b). After the anchoring of Cu species, the binding energy of N 1s shifted forward from the characteristic peak at 402.4 eV, and new characteristic peaks were generated [39]. These phenomena are consistent with the coordination reaction between Cu and N, and the schematic diagram exhibited in Fig. S4. There was no characteristic peak of Cu in the XPS result of Cu@U6N and Cu@U6N/ZIS (Fig. 4a). This suggested that trace amounts of Cu were anchored to the interior of the U6N channel and that no Cu species existed on the U6N outer surface, where could be detected by XPS. This phenomenon demonstrated that Cu@U6N/ZIS nanomaterials had a sandwich-like

Table 1

Analysis of textural properties of the different samples.

	BET Surface Area ^a (m^2/g)	Micropore size ^b (cm^3/g)	Total pore Volume ^b (cm^3/g)	Pore Size (nm)
U6N	1068.7	0.38	0.5	0.58, 1.30
Cu@U6N	1166.8	0.4	0.51	0.60, 1.30
Cu@U6N/ZIS	188.5	0.06	0.19	0.64, 1.24
ZIS	68.7	—	0.26	14.9

^a Calculated by BET method.

^b Single point adsorption total pore volume of pores less than 193.4646 nm diameter at $P/P_0 = 0.990000000$.

three-layered structure, which offered the possibility of providing different reaction sites for organic pollutant degradation and hydrogen production.

To investigate the role of U6N pore structure in the simultaneous photocatalytic degradation of phenol and hydrogen production system, the specific surface area and the pore size distribution of the material were analyzed by N_2 adsorption-desorption measurements. As shown in Fig. 5a, U6N and Cu@U6N displayed typical type I isotherms, and the amount of adsorbed N_2 increased sharply in the low-pressure section, suggesting microporous structures. The BET surface area and pore size distributions of U6N and Cu@U6N were very similar (Fig. 5a and Table 1), indicating that the incorporation of Cu species had a limited effect on U6N. In addition, Cu anchored on U6N did not block the U6N channel, but the micropore size and pore volume of Cu@U6N were slightly increased, confirming that the preparation method successfully dispersed Cu species.

The N_2 adsorption isotherm of ZIS showed a type II isotherm, which is consistent with its multilayer dispersed structure. The Cu@U6N/ZIS photocatalyst exhibited hybrid I/IV isotherms with an obvious hysteresis loop, indicating that there were both micropores and mesoporous structures in the composite. According to the micropore size distribution in Fig. 5b and Table 1, the diameters of the tetrahedral and octahedral cage structures of U6N were 0.58 nm and 1.30 nm, respectively, which were consistent with the theoretical simulation values of UiO-66- NH_2 [40]. The diameters of tetrahedral and octahedral cage structures of Cu@U6N were 0.60 nm and 1.30 nm, respectively. According to the literature [41,42], the molecular size of phenol was 0.68 nm, which was larger than the window size of the cage structure in Cu@U6N (Fig. S5). As a result, only the anchored Cu in Cu@U6N could become the reduction site of hydrogen evolution, which would be physically separated from the oxidation site of the phenol degradation.

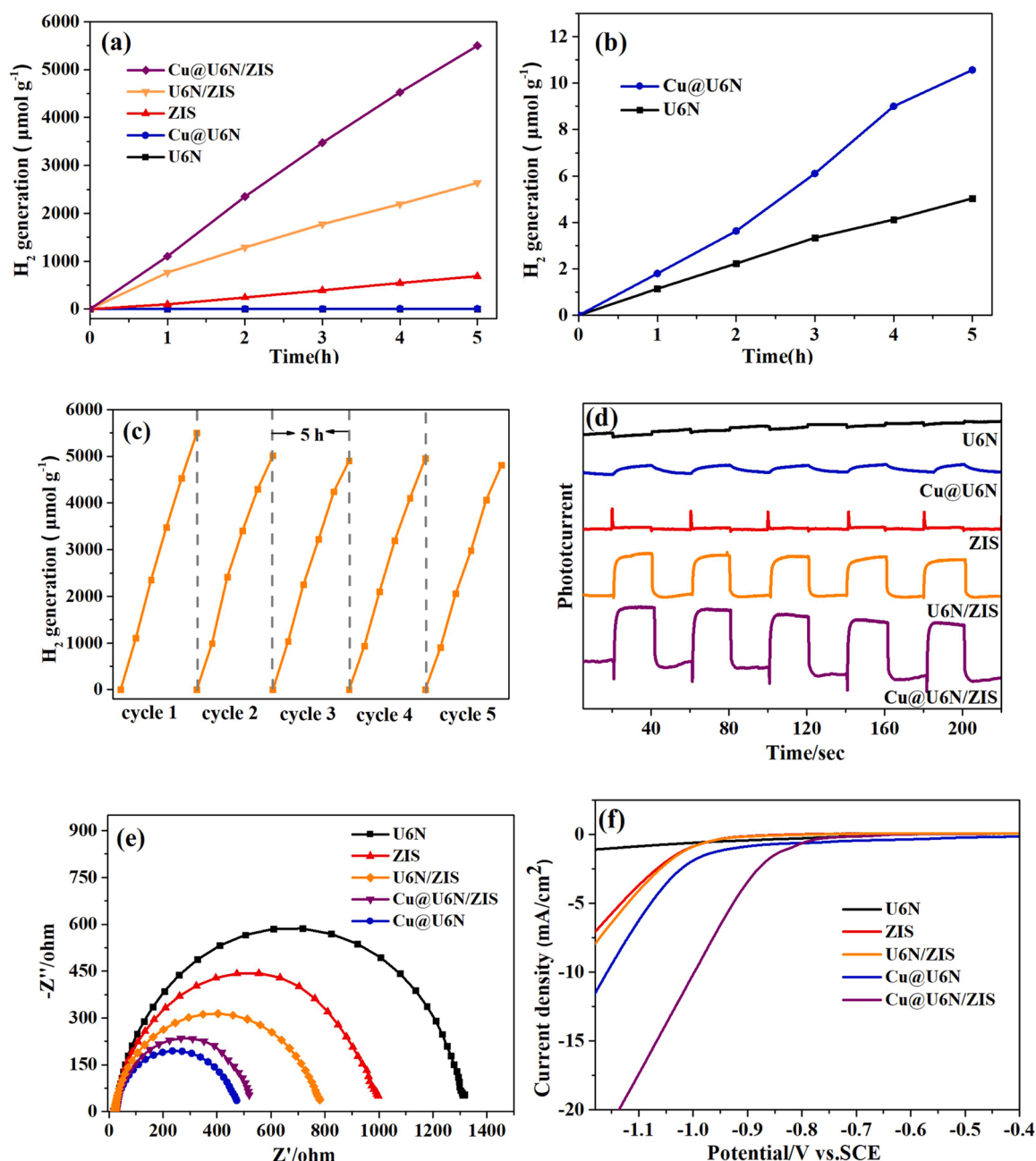


Fig. 6. (a-b) Time courses of photocatalytic H_2 evolution over different samples under visible light irradiation, and (c) cycling stability of Cu@U6N/ZIS. (d) Transient photocurrent spectra, (e) EIS spectra, and (f) LSV polarization curves of different samples.

3.2. Photocatalytic activity and photoelectrochemical (PEC) properties

To evaluate the photocatalytic activity of the synthesized samples, triethanolamine (TEOA) was used as a hole sacrificial agent. Fig. 6a and b show that the hydrogen production curves of the samples displayed excellent linearity. Among them, only pristine U6N did not exhibit any significant photocatalytic activity ($1 \mu\text{mol g}^{-1} \text{h}^{-1}$). The hydrogen production rate was significantly increased after Cu was anchored by the photoinduction method, owing to the enrichment of electrons on Cu and the abundant hydrogen evolution sites provided by Cu. ZIS also presented low hydrogen evolution rates ($100 \mu\text{mol g}^{-1} \text{h}^{-1}$). The U6N/ZIS displayed significantly higher hydrogen evolution rate than U6N or ZIS, which was attributed to the formation of heterojunctions between U6N and ZIS, thereby promoting the separation of electron-hole pairs. Compared to the samples with only internal (Cu@U6N) or external

(U6N/ZIS) modification, Cu@U6N/ZIS with three layers of sandwich structure exhibited the highest hydrogen production activity of $1158 \mu\text{mol g}^{-1} \text{h}^{-1}$, which was about 1000 times and 11 times higher than that of pure U6N and pure ZIS, respectively. This large enhancement was attributed to the fact that Cu@U6N/ZIS may have a directional electron transfer path from the outside to the inside, which could effectively inhibit the recombination of electron-hole pairs, leading to more reduction reactions and hydrogen production.

Cyclic stability is one of the key factors characterizing the performance of photocatalysts. Therefore, the Cu@U6N/ZIS nanocomposite was operated for five reactive cycles under consecutive 5 h irradiation runs. The hydrogen evolution in every five-hour-reaction was nearly unchanged (Fig. 6c), indicative of stability and good recyclability of the Cu@U6N/ZIS photocatalyst. Moreover, after photocatalytic reaction for five cycles, the morphology and the crystalline structure of the

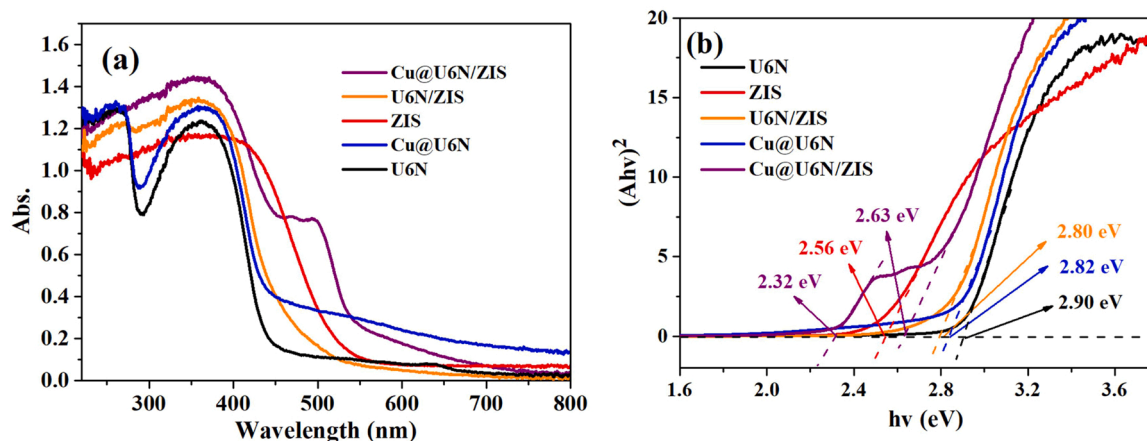


Fig. 7. (a) UV-vis spectra, and (b) the plots of transformed Kubelka-Munk function versus the light energy.

Cu@U6N/ZIS sample were determined by SEM and XRD (Fig. S6), respectively. These results are consistent with the observed stable performance of Cu@U6N/ZIS.

To study the photogenerated carrier migration and transfer efficiency, the photocurrent response was investigated. The results are shown in Fig. 6d. Compared with U6N, ZIS, Cu@U6N, and U6N/ZIS, Cu@U6N/ZIS composites had the highest transient photocurrent responses, indicating that Cu@U6N/ZIS had stronger light absorption and lower photogenerated carrier recombination. There was a significant delay in the Cu@U6N photocurrent response compared to that of U6N. This observation is consistent with the hypothesis that Cu species could effectively enrich photogenerated electrons and inhibit the recombination of electron-hole pairs, in part, because the Cu was the active site for hydrogen evolution.

To characterize the charge carrier transportation, electrochemical impedance spectroscopy (EIS) analysis was performed (Fig. 6e). Cu@U6N and Cu@U6N/ZIS composites had similar arc radii and were much smaller than that of U6N, ZIS, and U6N/ZIS. This was due to the coordination of Cu with amino groups, achieving high dispersion of Cu, which could improve the efficiency of charge transfer over charge recombination. The results of the linear sweep voltammetry (LSV) curves demonstrated that anchored Cu species could significantly reduce the hydrogen evolution overpotential of U6N and U6N/ZIS (Fig. 6f). The high dispersion of Cu species, which are sites of hydrogen evolution, increased the photocatalytic hydrogen production reaction.

UV-vis spectroscopy was used to investigate the light absorption characteristics of different photocatalysts (Fig. 7a). Pristine U6N and ZIS exhibited an absorption edge at 443 and 532 nm, corresponding to bandgap energies of 2.90 and 2.56 eV, respectively (Fig. 7b). The light

absorption of U6N/ZIS was slightly stronger in both visible and ultra-violet regions. Compared with U6N and U6N/ZIS, the addition of Cu could narrow the band gap and promote the visible light absorption in Cu@U6N and Cu@U6N/ZIS composites. Cu@U6N/ZIS displayed two obvious absorption edges belonging to Cu@U6N and ZIS. It should be noted that the calculated bandgap energy of Cu@U6N and ZIS in Cu@U6N/ZIS were different from their individual bandgaps, indicating that there was a close contact interface between Cu@U6N and ZIS, as well as electrostatic attraction and interaction after in-situ synthesis of the composite.

3.3. Dual photocatalytic activity and toxicity assessment

To investigate simultaneous photocatalytic hydrogen production and organic pollutants photodegradation, we chose various phenolic compounds and antibiotics as common organics pollutants, including sulfadiazine (SDZ), ciprofloxacin (CIP), tetracycline hydrochloride (TC), phenol, hydroquinone (HQ), 2,4-dichlorophenol (2, 4-DCP), and bisphenol A (BPA). From Fig. 8a and Fig. S7, the photocatalytic hydrogen production rate was very low over Cu@U6N/ZIS in deionized water ($3.2 \mu\text{mol g}^{-1} \text{h}^{-1}$). When SDZ, HQ, and 2, 4-DCP were added into the photocatalytic system, the hydrogen evolution rate did not change significantly. In contrast, the addition of TC, CIP, and phenol in the photocatalytic system significantly increased the rate of hydrogen evolution. At the same time, the degradation efficiency of TC, CIP, and phenol was 80.6%, 47.6%, and 73.1%, respectively (Fig. 8b). The highest hydrogen production of $83.4 \mu\text{mol g}^{-1} \text{h}^{-1}$ was achieved when degrading phenol. Therefore, phenol was chosen to be the simulated pollutant in the following experiments of photocatalytic hydrogen

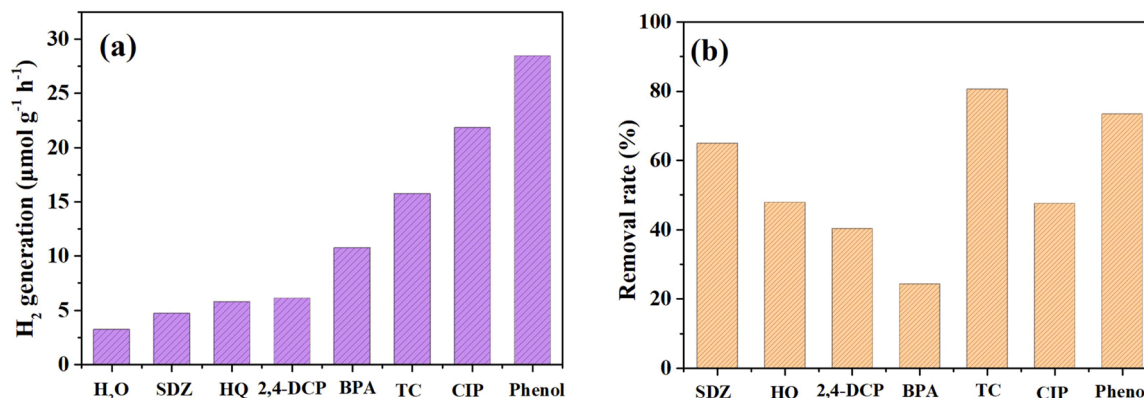


Fig. 8. Simultaneous photocatalytic H_2 evolution and the degradation efficiency of different pollutants over Cu@U6N/ZIS.

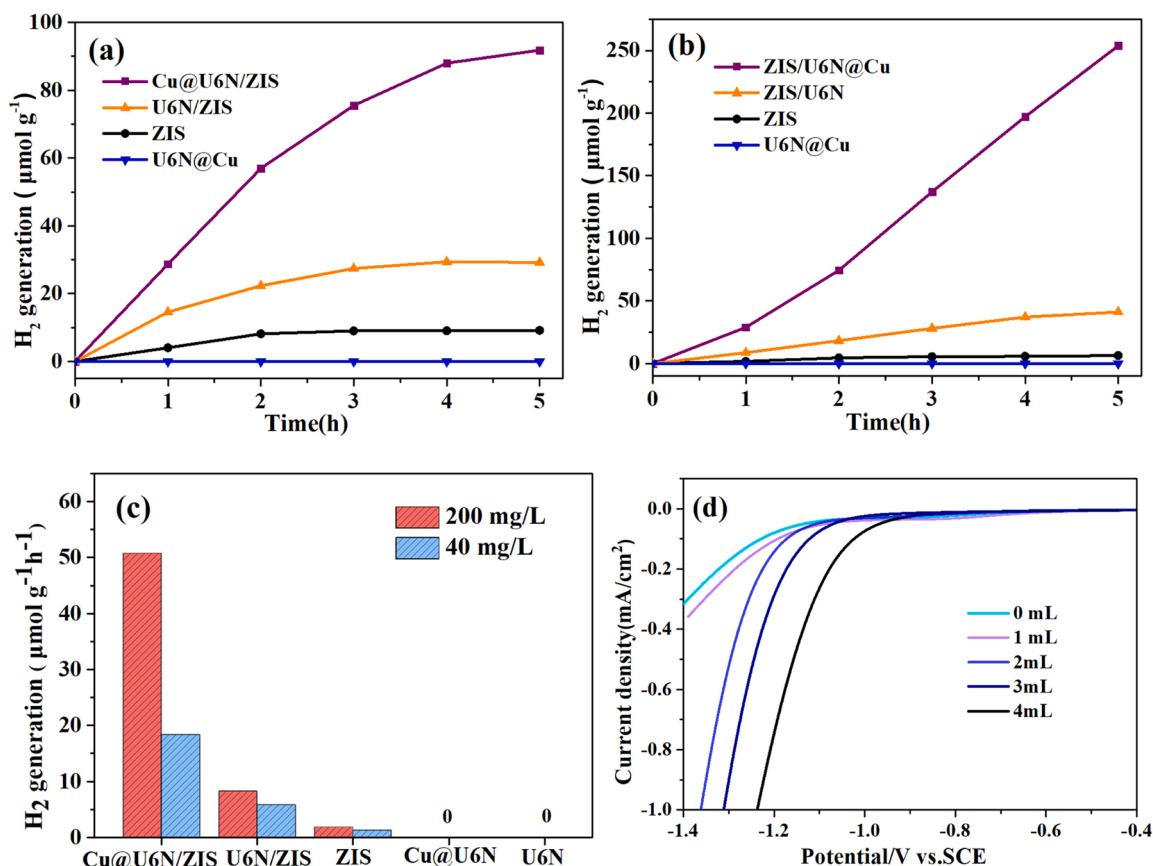


Fig. 9. Time courses of photocatalytic H_2 evolution over different samples with different concentrations of phenol: (a) 40 mg/L and (b) 200 mg/L, (c) Simultaneous photocatalytic H_2 evolution rate of the wastewater containing different concentrations of phenol, and (d) LSV curves of Cu@U6N/ZIS added with different amounts of phenol solution (40 mg/L).

production.

At a phenol concentration of 40 mg/L (Fig. 9a), the hydrogen production rate of Cu@U6N/ZIS was initially low and soon plateaued. However, at a higher concentration (200 mg/L) the hydrogen production was increased over a long period of time (Fig. 9b). The hydrogen production rate results are shown in Fig. 9c. In contrast, there was no significant change observed in the hydrogen production rate of ZIS at different concentrations. The hydrogen production rate of U6N/ZIS at high concentration was about 1.5 times than that at low concentrations, while the rate with Cu@U6N/ZIS reached 3 times the rate at the low concentrations. These results implied that the three-layered material was favorable to the synergistic reaction. The blocking of phenol molecules by U6N cage window and the anchoring of Cu in U6N created space and sites only for the reduction reaction, effectively improving the rate of photocatalytic hydrogen production. In addition, the LSV curves of Cu@U6N/ZIS were tested at different concentrations of phenol. Fig. 9d shows that the addition of phenol reduced the initial overpotential, favoring the occurrence of the half-reaction of hydrogen evolution.

The trapping experiments of radical species ($\bullet O_2^-$, $\bullet OH$ and h^+) was carried out to explore the mechanism of Cu@U6N/ZIS for degradation of phenol under the coupled system. BQ/IPA/TEOA were selected as the scavengers of $\bullet O_2^-/\bullet OH/h^+$, respectively. When TEOA was added, it obviously inhibited the remove of phenol (Fig. S8). The experimental results demonstrated that the main active oxygen species (h^+) required for the photodegradation of phenol was complementary to the species required for the photocatalytic generation of H_2 (e^-), thereby promoting the generation of H_2 .

To explore the process of the oxidation half-reaction, TOC and COD of the phenol solution before and after photocatalytic hydrogen

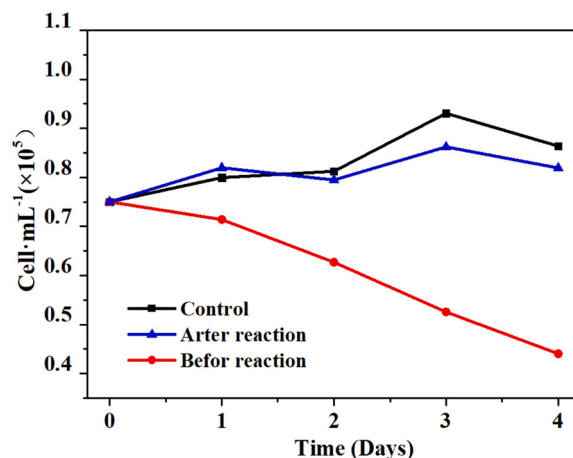


Fig. 10. Growth of *C. vulgaris* exposed to phenol solution collected before and after photocatalytic degradation.

production were tested at the low concentration (40 mg/L) (Fig. S9). The results show that the removal rate of COD (75.7%) was much higher than that of TOC (15.3%) under the coupled system. This indicated that the process still failed to mineralize organic pollutants, but oxidized them. In the process of H^+ being reduced to hydrogen by electrons, phenol as the substrate was oxidized by holes and the process of bond breaking occurs. Since the reaction was carried out in anoxic environment (purged with N_2 for 30 min to remove dissolved oxygen), the phenol could not be deeply oxidized to CO_2 and H_2O . However, this

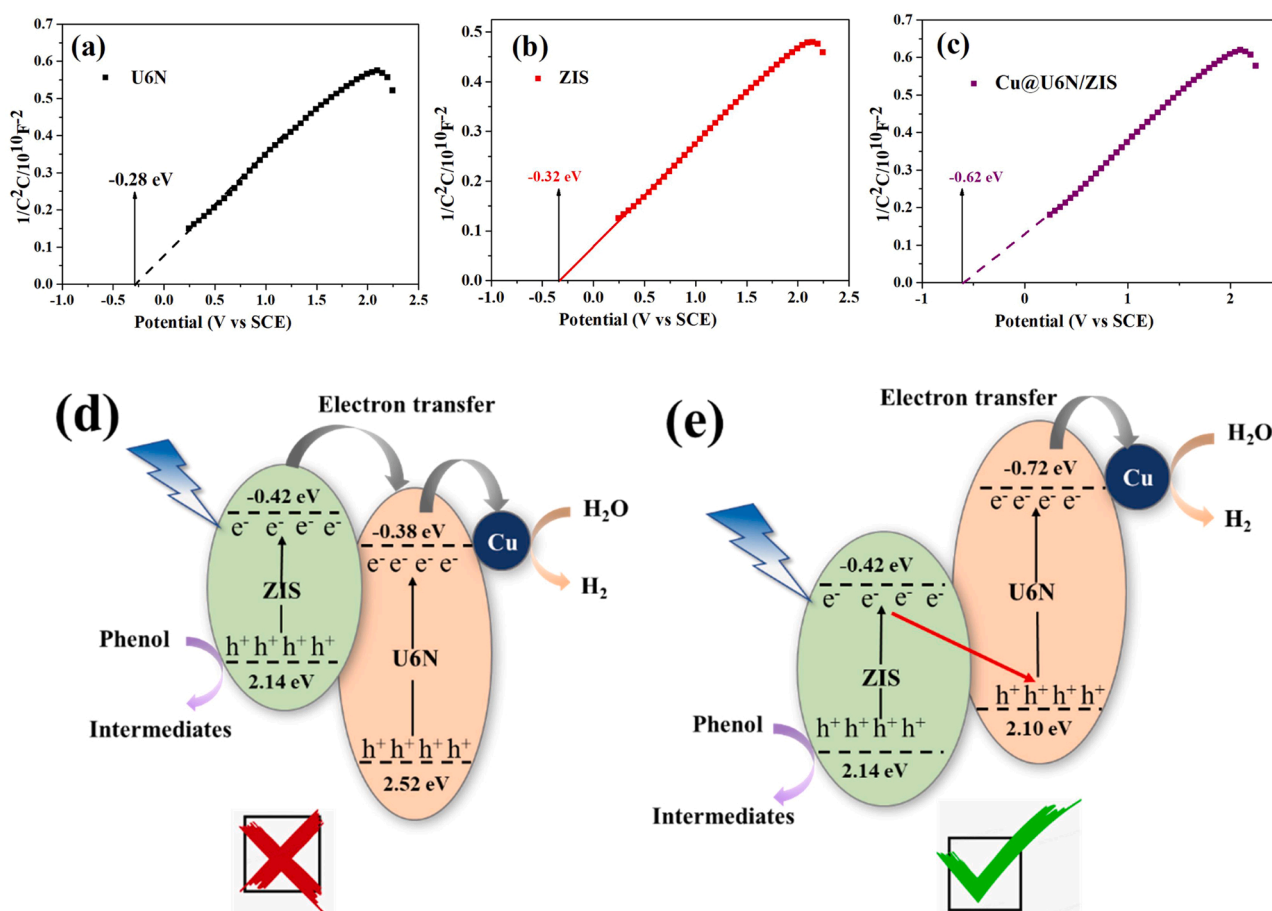


Fig. 11. (a-c) Mott-Schottky plot of different samples. Band structure and charge transfer mechanism of Cu@U6N/ZIS during hydrogen evolution and phenol photodegradation: (d) traditional type II and (e) direct Z-scheme.

resulted in a higher oxygen content ratio in the intermediate products, which would facilitate further oxidation. The phenol solution at the end of the hydrogen production process could eliminate TOC more quickly with Cu@U6N/ZIS. Under the same initial TOC concentration and reaction conditions, the TOC removal rate of phenol solution after hydrogen production was significantly increased (Fig. S10).

Although the coupled system could achieve continuous hydrogen production and improve the quality of simulated wastewater, its environmental benefits still needed to be evaluated. Therefore, the aquatic toxicity of phenol wastewater before and after the hydrogen production reaction was investigated using *Chlorella vulgaris* as an ecological indicator. The concentration of *Chlorella vulgaris* was measured daily by UV-vis spectrometer at 680 nm (Fig. S11). For the control group, the cell density of *Chlorella vulgaris* increased after 4 days of cultivation (Fig. 10). In untreated phenol solution, cell density decreased significantly, indicating that phenol had obvious biological toxicity. The inhibition of *Chlorella vulgaris* growth by phenol solution was significantly weakened after the photocatalytic coupled system. Thus, the biological toxicity of phenol could be effectively reduced in the simulated process of hydrogen energy recovery from wastewater under sunlight irradiation. This was benefited to further oxidation, improved the biodegradability of the wastewater by reducing toxicity, and also facilitated the biological wastewater treatment process. In addition, the oxidation products of phenol were retained in the wastewater, instead of forming CO_2 in the gaseous phase, which was mixed with H_2 , improving the purity of the value-added products. This study suggests new avenues for environmental restoration and non-fossil fuel production.

3.4. The charge transfer pathway and possible photocatalytic mechanism

In order to investigate the electron transfer path in Cu@U6N/ZIS composite, the conduction band and valence band positions of each component in the material were measured. First, the electrochemical flat potential of U6N and ZIS was determined by the Mott-Schottky plots. The slope of obtained curves was positive, validating their typical n-type semiconductor nature. The flat band position of U6N and ZIS was -0.28 and -0.32 eV vs NHE, respectively (Fig. 11a and b). The conduction band (CB) potential of n-type semiconductors is 0.1–0.2 eV above the flat band potential [16]. Thus, the CBs of U6N and ZIS were estimated as -0.38 and -0.42 eV, respectively. Then, concerning the bandgap positions obtained in Fig. 7b, we can draw the energy diagram of lowest unoccupied molecular orbital (LUMO) and highest occupied molecular orbital (HOMO) levels of U6N, and the energy diagram of the VB and CB levels of ZIS (Fig. 11d). If possible conventional type II electron transport paths were formed, then the electrons could migrate from the CB of ZIS to LUMO of U6N and the holes could migrate from HOMO of U6N to the VB of ZIS.

However, the CB levels of Cu@U6N/ZIS composite was -0.72 eV determined by Mott-Schottky tests (Fig. 11c), which was more negative than that of U6N and ZIS. Therefore, Cu@U6N/ZIS composites had superior reduction properties. Further, the Z-scheme charge transfer model was proposed for the energy level rise process of the Cu@U6N/ZIS composites (Fig. 11e). Under simulated sunlight irradiation, both U6N and ZIS could be excited and generate electrons and holes. Because of the intimate interfacial contact between U6N and ZIS, strong electrostatic attraction existed between the electrons in CB of ZIS and holes in HOMO of U6N, thereby the photogenerated electrons in the CB of ZIS

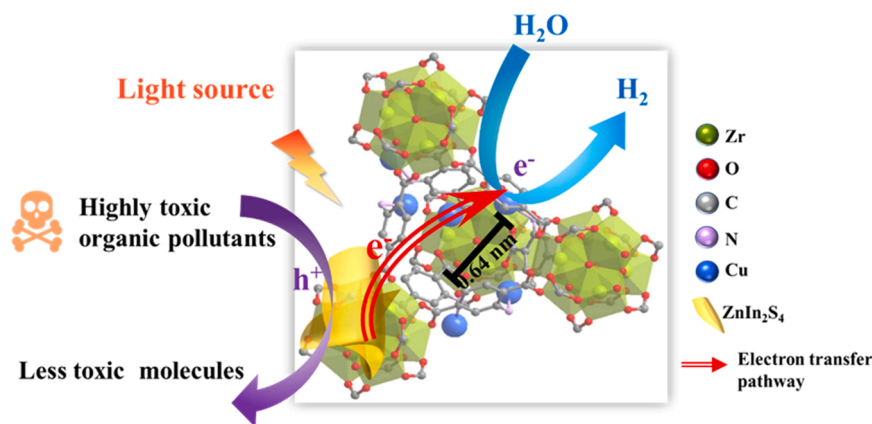


Fig. 12. The proposed mechanism of simultaneously photocatalytic hydrogen generation and phenol photodegradation over Cu@U6N/ZIS.

were inclined to be directly transferred into the HOMO of U6N. Subsequently, the electrons retained in the LUMO of U6N were further enriched on Cu species inside U6N. The highly dispersed Cu species served as active sites using electrons to evolve hydrogen (Fig. 12). At the same time, the holes left by the VB end of ZIS degraded the phenol blocked on the outside of U6N window. The directed migration of electrons effectively inhibited the recombination of electron-hole pairs. In short, the special three-layered structure of Cu@U6N/ZIS created different locations for sites of the oxidation and reduction reactions and improved the utilization of electron holes, thus contributing to the overall enhanced photocatalytic rate.

4. Conclusions

In summary, a novel photocatalyst was successfully synthesized through two steps: Cu species was anchored to the amino group in U6N by photoinduction, and then ZnIn₂S₄ nanosheets were wrapped around U6N using a simple solvothermal method. The externally wrapped ZIS had a close contact interface with U6N, forming Z-type heterojunctions, while the Cu species inside U6N effectively enriched for electrons and provided sufficient reaction sites for hydrogen production. The sandwich-like structure facilitated charge separation from photo-generated electrons and their holes. By coupling photocatalytic hydrogen production with organic pollutants degradation, a non-fossil fuel was generated while a toxic pollutant was removed without the consumption of expensive sacrificial agents. This study provides a new approach for the design of dual-function photocatalysts that combine energy development and environmental remediation and risk reduction.

CRediT authorship contribution statement

Sijia Liu: Conceptualization, Investigation, Methodology, Validation, Data curation, Writing – original draft. **Xifei Zhou:** Investigation, Data curation. **Changqing Yang:** Conceptualization, Methodology. **Chaohai Wei:** Supervision, Methodology. **Yun Hu:** Supervision, Methodology, Financial Support, Writing – review & editing.

Declaration of Competing Interest

The authors declare that they have no known competing financial interests or personal relationships that could have appeared to influence the work reported in this paper.

Data availability

No data was used for the research described in the article.

Acknowledgments

This work was supported by Science and Technology Project of Guangdong Province (2022A0505050002) and Scientific Research Project of Guangzhou City (201804020026).

Appendix A. Supporting information

Supplementary data associated with this article can be found in the online version at doi:10.1016/j.apcatb.2023.122572.

References

- [1] C. Bie, L. Wang, J. Yu, Challenges for photocatalytic overall water splitting, *Chem* 8 (2022) 1567–1574.
- [2] T. Takata, J. Jiang, Y. Sakata, M. Nakabayashi, N. Shibata, V. Nandal, K. Seki, T. Hisatomi, K. Domen, Photocatalytic water splitting with a quantum efficiency of almost unity, *Nature* 581 (2020) 411–414.
- [3] M. Wen, K. Mori, Y. Futamura, Y. Kuwahara, M. Navlani-Garcia, T. An, H. Yamashita, PdAg nanoparticles within core-shell structured zeolitic imidazolate framework as a dual catalyst for formic acid-based hydrogen storage/production, *Sci. Rep.* 9 (2019) 15675–15685.
- [4] H. Chen, Z.G. Gu, S. Mirza, S.H. Zhang, J. Zhang, Hollow Cu–TiO₂/C nanospheres derived from a Ti precursor encapsulated MOF coating for efficient photocatalytic hydrogen evolution, *J. Mater. Chem. A* 6 (2018) 7175–7181.
- [5] B. Cao, G. Li, H. Li, Hollow spherical RuO₂@TiO₂@Pt bifunctional photocatalyst for coupled H₂ production and pollutant degradation, *Appl. Catal. B Environ.* 194 (2016) 42–49.
- [6] S. Kampouri, K.C. Stylianou, Dual-functional photocatalysis for simultaneous hydrogen production and oxidation of organic substances, *ACS Catal.* 9 (2019) 4247–4270.
- [7] Y. Wu, Y. Li, H. Hu, G. Zeng, C. Li, Recovering hydrogen energy from photocatalytic treatment of pharmaceutical-contaminated water using Co₃O₄ modified {001}/[101]-TiO₂ nanosheets, *ACS EST Engg* 1 (2021) 603–611.
- [8] S. Liu, Z. Zhang, F. Huang, Y. Liu, L. Feng, J. Jiang, L. Zhang, F. Qi, C. Liu, Carbonized polyaniline activated peroxydisulfate (PMS) for phenol degradation: role of PMS adsorption and singlet oxygen generation, *Appl. Catal. B Environ.* 286 (2021) 119921–119933.
- [9] F.X. Dong, L. Yan, X.H. Zhou, S.T. Huang, J.Y. Liang, W.X. Zhang, Z.W. Guo, P. R. Guo, W. Qian, L.J. Kong, W. Chu, Z.H. Diao, Simultaneous adsorption of Cr(VI) and phenol by biochar-based iron oxide composites in water: performance, kinetics and mechanism, *J. Hazard. Mater.* 416 (2021) 125930–125941.
- [10] L. Qin, W. Chen, Y. Fu, J. Tang, H. Yi, L. Li, F. Xu, M. Zhang, W. Cao, D. Huang, C. Lai, Hemin derived iron and nitrogen-doped carbon as a novel heterogeneous electro-Fenton catalyst to efficiently degrade ciprofloxacin, *Chem. Eng. J.* 449 (2022) 137840–137851.
- [11] Y. Xue, M. Kamali, X. Yu, L. Appels, R. Dewil, Novel CuO/Cu₂(V₂O₇)/V₂O₅ composite membrane as an efficient catalyst for the activation of persulfate toward ciprofloxacin degradation, *Chem. Eng. J.* 449 (2022) 137840–137851.
- [12] L. Seid, D. Lakhdari, M. Berkani, O. Belgherbi, D. Chouder, Y. Vasseghian, N. Lakhdari, High-efficiency electrochemical degradation of phenol in aqueous solutions using Ni-PPy and Cu-PPy composite materials, *J. Hazard. Mater.* 423 (2022) 126986–126998.
- [13] A. Smaali, M. Berkani, F. Merouane, V.T. Le, Y. Vasseghian, N. Rahim, M. Kouachi, Photocatalytic-persulfate-oxidation for diclofenac removal from aqueous solutions: modeling, optimization and biotoxicity test assessment, *Chemosphere* 266 (2021) 129158–129173.

- [14] Y. Vasseghian, M. Berkani, F. Almomani, E.N. Dragoi, Data mining for pesticide decontamination using heterogeneous photocatalytic processes, *Chemosphere* 270 (2021) 129449–129463.
- [15] C. Chen, H. Zeng, M. Yi, G. Xiao, S. Xu, S. Shen, B. Feng, In-situ growth of Ag_3PO_4 on calcined Zn-Al layered double hydroxides for enhanced photocatalytic degradation of tetracycline under simulated solar light irradiation and toxicity assessment, *Appl. Catal. B Environ.* 252 (2019) 47–54.
- [16] Y. Hu, J. Zhang, J. Qin, Z. Yang, M. Fu, TiO_2 -UiO-66- NH_2 nanocomposites as efficient photocatalysts for the oxidation of VOCs, *Chem. Eng. J.* 385 (2020) 123814–123827.
- [17] Z. Yang, Z. Guo, J. Zhang, Y. Hu, The development and application of metal-organic frameworks in the field of photocatalysis, *Res. Chem. Inter.* 47 (2021) 325–343.
- [18] M. Wen, G. Li, H. Liu, J. Chen, T. An, H. Yamashita, Metal-organic framework-based nanomaterials for adsorption and photocatalytic degradation of gaseous pollutants: recent progress and challenges, *Environ. Sci. Nano* 6 (2019) 1006–1025.
- [19] C. Zhao, X. Pan, Z. Wang, C.C. Wang, $1 + 1 > 2$: a critical review of MOF/bismuth-based semiconductor composites for boosted photocatalysis, *Chem. Eng. J.* 417 (2021) 128022–128056.
- [20] L. Shen, R. Liang, L. Wu, Strategies for engineering metal-organic frameworks as efficient photocatalysts, *Chin. J. Catal.* 36 (2015) 2071–2088.
- [21] Y. Pei, J. Qin, J. Wang, Y. Hu, Fe-based metal organic framework derivative with enhanced Lewis acidity and hierarchical pores for excellent adsorption of oxygenated volatile organic compounds, *Sci. Total Environ.* 790 (2021) 148132–148143.
- [22] S. Liu, X. Zhou, C. Wei, Y. Hu, Spatial directional separation and synergetic treatment of Cr(VI) and Rhodamine B mixed pollutants on three-layered Pd@MIL-101/P25 photocatalyst, *Sci. Total. Environ.* 842 (2022) 156836–156847.
- [23] S. You, Y. Hu, X. Liu, C. Wei, Synergetic removal of Pb(II) and dibutyl phthalate mixed pollutants on Bi_2O_3 - TiO_2 composite photocatalyst under visible light, *Appl. Catal. B Environ.* 232 (2018) 288–298.
- [24] F. Xing, C. Cheng, J. Zhang, Q. Liu, C. Chen, C. Huang, Tunable charge transfer efficiency in HxMoO_3 @ ZnIn_2S_4 hierarchical direct Z-scheme heterojunction toward efficient visible-light-driven hydrogen evolution, *Appl. Catal. B Environ.* 285 (2021) 119818–119829.
- [25] Y. Chao, P. Zhou, N. Li, J. Lai, Y. Yang, Y. Zhang, Y. Tang, W. Yang, Y. Du, D. Su, Y. Tan, S. Guo, Ultrathin visible-light-driven mo incorporating In_2O_3 - ZnIn_2S_4 Z-Scheme nanosheet photocatalysts, *Adv. Mater.* 31 (2019) 1807226–1807233.
- [26] Y. Qin, H. Li, J. Lu, Y. Feng, F. Meng, C. Ma, Y. Yan, M. Meng, Synergy between van der waals heterojunction and vacancy in ZnIn_2S_4 /g- C_3N_4 2D/2D photocatalysts for enhanced photocatalytic hydrogen evolution, *Appl. Catal. B Environ.* 277 (2020) 119254–119264.
- [27] L. Wang, B. Cheng, L. Zhang, J. Yu, In situ Irradiated XPS Investigation on S-Scheme TiO_2 @ ZnIn_2S_4 photocatalyst for efficient photocatalytic CO_2 reduction, *Small* 17 (2021) 2103447–2103456.
- [28] R. Yang, L. Mei, Y. Fan, Q. Zhang, R. Zhu, R. Amal, Z. Yin, Z. Zeng, ZnIn_2S_4 -based photocatalysts for energy and environmental applications, *Small Methods* 5 (2021) 2100887–2100947.
- [29] X. Peng, L. Ye, Y. Ding, L. Yi, C. Zhang, Z. Wen, Nanohybrid photocatalysts with ZnIn_2S_4 nanosheets encapsulated UiO-66 octahedral nanoparticles for visible-light-driven hydrogen generation, *Appl. Catal. B Environ.* 260 (2020) 118152–118161.
- [30] X.B. Meng, J.L. Sheng, H.L. Tang, X.J. Sun, H. Dong, F.-M. Zhang, Metal-organic framework as nanoreactors to co-incorporate carbon nanodots and CdS quantum dots into the pores for improved H_2 evolution without noble-metal cocatalyst, *Appl. Catal. B Environ.* 244 (2019) 340–346.
- [31] G. Wang, C.T. He, R. Huang, J. Mao, D. Wang, Y. Li, Photoinduction of Cu single atoms decorated on UiO-66- NH_2 for enhanced photocatalytic reduction of CO_2 to liquid fuels, *J. Am. Chem. Soc.* 142 (2020) 19339–19345.
- [32] S. Mao, J.W. Shi, G. Sun, D. Ma, C. He, Z. Pu, K. Song, Y. Cheng, Au nanodots@thiol-UiO66@ ZnIn_2S_4 nanosheets with significantly enhanced visible-light photocatalytic H_2 evolution: the effect of different Au positions on the transfer of electron-hole pairs, *Appl. Catal. B Environ.* 282 (2021) 119550–119560.
- [33] M. Wen, S. Song, Q. Liu, H. Yin, K. Mori, Y. Kuwahara, G. Li, T. An, H. Yamashita, Manipulation of plasmon-induced hot electron transport in Pd/ MoO_3 -x@ZIF-8: boosting the activity of Pd-catalyzed nitroaromatic hydrogenation under visible-light irradiation, *Appl. Catal. B Environ.* 282 (2021) 119511–119519.
- [34] A.A. Dubale, I.N. Ahmed, X.-H. Chen, C. Ding, G.-H. Hou, R.F. Guan, X. Meng, X. L. Yang, M.H. Xie, A highly stable metal-organic framework derived phosphorus doped carbon/Cu $_2\text{O}$ structure for efficient photocatalytic phenol degradation and hydrogen production, *J. Mater. Chem. A* 7 (2019) 6062–6079.
- [35] T. Gu, W. Teng, N. Bai, Z. Chen, J. Fan, W.-x Zhang, D. Zhao, Nano-spatially confined Pd-Cu bimetal in porous N-doped carbon as an electrocatalyst for selective denitrification, *J. Mater. Chem. A* 8 (2020) 9545–9553.
- [36] X. Chen, S. Xiao, H. Wang, W. Wang, Y. Cai, G. Li, M. Qiao, J. Zhu, H. Li, D. Zhang, Y. Lu, MOFs conferred with transient metal centers for enhanced photocatalytic activity, *Angew. Chem. Int. Ed. Engl.* 59 (2020) 17182–17186.
- [37] X.Y. Dong, M. Zhang, R.B. Pei, Q. Wang, D.H. Wei, S.Q. Zang, Y.T. Fan, T.C. Mak, A crystalline copper(ii) coordination polymer for the efficient visible-light-driven generation of hydrogen, *Angew. Chem. Int. Ed. Engl.* 55 (2016) 2073–2077.
- [38] J.H. Cavka, S. Jakobsen, U. Olsbye, N. Guillou, C. Lamberti, S. Bordiga, K. Lillerud, A new zirconium inorganic building brick forming metal organic frameworks with exceptional stability, *J. Am. Chem. Soc.* 130 (2008) 13850–13851.
- [39] X. Fang, S. Wu, Y. Wu, W. Yang, Y. Li, J. He, P. Hong, M. Nie, C. Xie, Z. Wu, K. Zhang, L. Kong, J. Liu, High-efficiency adsorption of norfloxacin using octahedral UiO-66- NH_2 nanomaterials: dynamics, thermodynamics, and mechanisms, *Appl. Surf. Sci.* 518 (2020) 146226–146236.
- [40] Y. Han, M. Liu, K. Li, Y. Zuo, Y. Wei, S. Xu, G. Zhang, C. Song, Z. Zhang, X. Guo, Facile synthesis of morphology and size-controlled zirconium metal-organic framework UiO-66: the role of hydrofluoric acid in crystallization, *CrystEngComm* 17 (2015) 6434–6440.
- [41] T. Kawai, K.J.C. Tsutsumi, P. Science, Adsorption characteristics of surfactants and phenol on modified zeolites from their aqueous solutions, *Colloid Polym. Sci.* 273 (1995) 787–792.
- [42] S. Inagaki, Y. Tsuboi, M. Sasaki, K. Mamiya, S. Park, Y. Kubota, Enhancement of para-selectivity in the phenol oxidation with H_2O_2 over Ti-MCM-68 zeolite catalyst, *Green Chem.* 18 (2016) 735–741.